

# X-ray Fluorescence Nanotomography on Cometary Matter from Comet 81P/Wild2 Returned by Stardust

Geert Silversmit,<sup>†</sup> Bart Vekemans,<sup>†</sup> Frank E. Brenker,<sup>‡</sup> Sylvia Schmitz,<sup>‡</sup> Manfred Burghammer,<sup>§</sup> Christian Riekel,<sup>§</sup> and Laszlo Vincze<sup>\*,†</sup>

X-ray Microspectroscopy and Imaging Research Group, Department of Analytical Chemistry, Ghent University, Krijgslaan 281 S12, B-9000 Gent, Belgium, GeoScience Institute, Goethe University, Altenhöferallee 1, D-60438 Frankfurt am Main, Germany, and European Synchrotron Radiation Facility (ESRF), BP 220, F-38043 Grenoble CEDEX, France

Using a significantly improved method for X-ray fluorescence (XRF) tomography with submicrometer spatial resolution, the fully three-dimensional (3D) distribution of main and trace elements from calcium to selenium was determined at a spatial resolution level of 200 nm within a unique ( $\sim 2 \mu\text{m}$ ) comet coma particle brought to Earth by the National Aeronautical and Space Administration (NASA)'s Stardust mission. The measurements were based on synchrotron radiation XRF nanotomography that has been applied to the terminal particle located in an aerogel host, which was used to capture comet and interstellar grain particles in space. Using a symmetric dual-detector arrangement for the presented nano-XRF tomography measurements, a rotation angle of  $180^\circ$  was sufficient for the tomographic reconstruction. Dedicated correction algorithms were developed to correct for submicrometer-level distortions within the tomographic dataset arising from instabilities of the sample positioning system during data collection.

The National Aeronautical and Space Administration (NASA)'s Stardust spacecraft was designed to collect and bring comet coma particles and interstellar grains from Comet 81P/Wild2 to Earth. After a journey of 7 years in space, the Sample Return Capsule returned to Earth on January 15, 2006. The successful recovery of the Sample Return Capsule initiated an extensive study of this unique extraterrestrial material using various microanalytical and nanoanalytical techniques.<sup>1–3</sup>

To be able to capture the comet coma and interstellar grain particles in space, aerogel collectors were used. Aerogel is a silica-based solid that has a porous, foamlike structure, of which 99.8 vol % is empty space, making this material  $\sim 1000$  times less dense than glass. The relative speed between the spacecraft and comet 81P/Wild2 during the flyby through the comet coma was  $\sim 6.1$  km/s.<sup>2</sup> During capture, coma particles entering the aerogel were

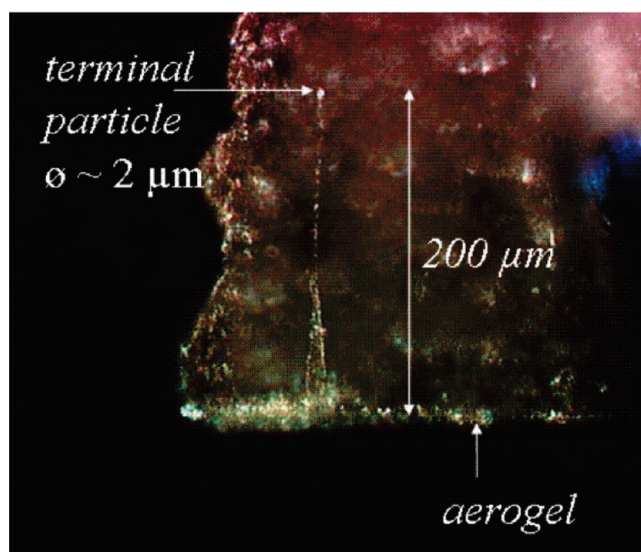


**Figure 1.** Optical microscope image of the impact track in the aerogel of the analyzed cometary grain, Stardust Track No. C2044,0,37.

stopped within a distance of typically a few hundred micrometers, creating carrot- and bulbous-shaped tracks inside the aerogel. The track and its terminal particle investigated by our team are shown in Figure 1.

The terminal particles of such impact tracks are typically a few micrometers in size. Therefore, submicrometer spatial resolution is needed to study, e.g., the variation of elemental composition within the individual comet coma particles. For the preliminary examination of this unique cometary matter, nondestructive in situ (as captured in the aerogel) techniques were applied. In this work, a novel fully three-dimensional (3D) nanoscopic synchrotron radiation X-ray fluorescence (nano SR-XRF) study was performed on the terminal particle of Stardust Track No. C2044,0,37 with a largest dimension of  $\sim 2 \mu\text{m}$ .

The high elemental sensitivity, nondestructive nature, and high spatial resolution provided by focused intense hard X-ray beams at second- and third-generation synchrotron facilities made synchrotron radiation (SR)-based microscopic X-ray fluorescence (micro-XRF) imaging of major, minor, and trace elements within various matrices an attractive microanalytical technique. By scanning the sample along a vertical and horizontal raster through the micro/nanobeam, two-dimensional (2D) projections of the

\* To whom correspondence should be addressed. Tel.: +32 9 264 48 22. Fax: +32 9 264 49 60. E-mail: Laszlo.Vincze@UGent.be.

<sup>†</sup> X-ray Microspectroscopy and Imaging Research Group, Department of Analytical Chemistry, Ghent University.

<sup>‡</sup> GeoScience Institute, JWU University.

<sup>§</sup> European Synchrotron Radiation Facility (ESRF).

(1) Burnett, D. S. *Science* 2006, 314, 1709–1710.

(2) Brownlee, D.; et al. *Science* 2006, 314, 1711–1716.

(3) Flynn, G. J.; et al. *Science* 2006, 314, 1731–1735.

elemental distributions within the sample can be obtained. The 2D elemental maps obtained this way contain no depth information, as the complete intersection of the beam with the sample is probed. However, depth information can be obtained by X-ray fluorescence (XRF) tomography. For XRF tomography, repetitive linear scans at a selected height in the sample are recorded for different rotation angles within a full angular range of  $0^{\circ}$ – $360^{\circ}$ . The different line profiles, as a function of the rotation angle, form so-called elemental sinograms. The in-plane elemental distribution (2D) can be reconstructed from the sinogram, which makes XRF tomography a nondestructive imaging technique that is able to visualize elemental distributions down to trace-level concentrations.<sup>4,5</sup> In contrast to confocal XRF imaging,<sup>6–8</sup> which is able to determine 3D elemental distributions with a resolution level limited by the acceptance of the applied polycapillary lens ( $\geq 10 \mu\text{m}$ ), the spatial resolution of XRF nanotomography is ultimately limited by the X-ray beam size that is used.

In our approach, presented below, this method has been generalized by collecting full 2D maps in the angular scan range, which allows the reconstruction of the 3D elemental distributions within this unique cometary matter.

Submicrometer beam sizes are becoming available at third-generation sources, opening up the possibility of XRF imaging and also XRF tomography at the nanoscopic level. Although more and more studies by nano-XRF start to appear, to our knowledge, no full 3D XRF tomography at the nanoscopic level has been reported so far. We present the first full three-dimensional nano-XRF tomography results with a spatial resolution of approximately 200 nm. The high spatial resolution provided by the beam puts stringent conditions on the accuracy and reproducibility of the sample positioning during linear and rotational scans. On the scale of the beam size ( $\sim 200 \text{ nm}$ ), considerable sample displacements can be expected, especially after each rotational movement, because of imperfections of the rotation axis and vertical drifts of the sample stage assembly due to gravity.

To be able to correct for such instabilities after data collection, instead of analyzing a single sample slice by conventional XRF tomographic (linear) scans, full 2D XRF projections were recorded at each observation angle. While more time-consuming than linear scans, this method allows for correction that is due to unavoidable sample positioning inaccuracies associated with rotational movements, and also gives the possibility of full 3D elemental reconstruction, instead of obtaining elemental distributions only in a single sample cross section.

The measured 2D projections typically suffer distortions, which can be characterized by submicrometer-scale vertical stretching (due to sample stage relaxation by gravity) and displacements in the vertical and horizontal direction. A rotational step especially induced a random change of the vertical and horizontal reference positions on the submicrometer level. This was partially corrected during the experiment itself, during which a fast prescanning technique was applied to optimize the relative beam position on

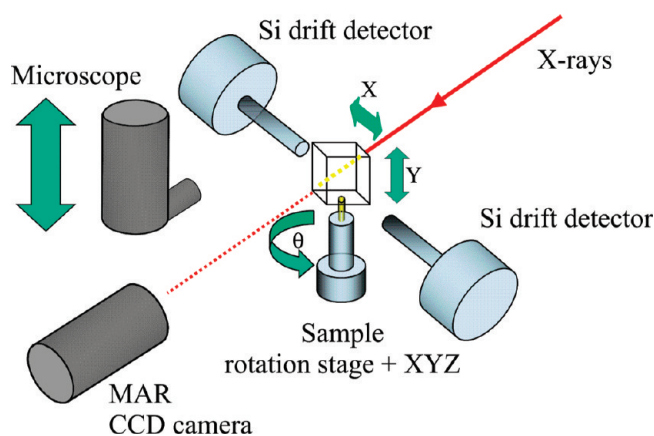


**Figure 2.** Schematic representation of the scanning XRF nanotomography setup installed at the Microfocus Beamline (ID13) of the European Synchrotron Radiation Facility (ESRF).

the sample before starting the next 2D scan at the new angle. To be able to perform the CT reconstruction, extra corrections on the vertical distortions and on the vertical and horizontal positions were needed. In what follows, the results of these corrections are described which demonstrate the feasibility of fully 3D nano-XRF tomography at a spatial resolution of 200 nm.

## EXPERIMENTAL SECTION

**The Synchrotron Nano-XRF Setup.** The synchrotron radiation nano-XRF measurements were performed at the ID13 Microfocus beamline of the European Synchrotron Radiation Facility (ESRF) in Grenoble, France. During this experiment, a liquid-nitrogen-cooled Si(111) double crystal monochromator was used to select an X-ray energy of 12.7 keV ( $\Delta E/E \approx 10^{-4}$ ). A submicrometer X-ray beam with dimensions of  $220 \text{ nm} \times 170 \text{ nm}$ , respectively (horizontal  $\times$  vertical, full width at half maximum (fwhm)), having an intensity of  $(4\text{--}5) \times 10^9$  photons/s was obtained using crossed linear Fresnel lens optics for beam focusing.<sup>9</sup>

The sample was mounted on a high-resolution piezo *xyz*-translation stage (NanoCube system manufactured by Physik Instrumente GmbH & Co., PI). This stage was installed on a vertical air-bearing rotation axis (UPR-160-Air, with  $\sim 1 \mu\text{m}$  eccentricity at the sample position, manufactured by Micos GmbH). A schematic drawing of the sample setup is given in Figure 2. The combined system enabled a translational positioning with a step resolution of  $\sim 10 \text{ nm}$ .

With respect to analytical characterization, the detection limits (DLs) achieved using the ID13 setup were determined using the geological reference material MPI-DING/ATHO-G<sup>10</sup> (rhyolite glass). The measured DL curves are given in Figures 3a and 3b. Absolute detection limits ranging from 500 ag (K) down to 5 ag (Zn) were achieved for a lifetime of 300 s. As shown by Figure 3b, the relative detection limits ranged from 40 ppm (K) to 400 ppb (Zn), using a data collection time of 300 s. For the typical duration of 1 s per pixel, in the case of our 2D scanning experiments, the effective absolute DLs ranged from 9 fg (K) to 90 ag (Zn) and relative DLs ranged from 700 ppm (K) down to 7

(4) Schröer, C. H. *Appl. Phys. Lett.* **2001**, *79*, 1912–1914.

(5) Golosio, B.; Simionovici, A.; Somogyi, A.; Lemelle, L.; Chukalina, M. *J. Appl. Phys.* **2003**, *94*, 145–156.

(6) Patterson, B. M.; Havrilla, G. J. *Am. Lab.* **2006**, *38*, 15.

(7) Kanniesser, B.; Malzer, W.; Reiche, I. *Nucl. Instrum. Methods Phys. Res., Sect. B* **2003**, *211*, 259–264.

(8) Vincze, L.; Vekemans, B.; Brenker, F. E.; Falkenberg, G.; Rickers, K.; Somogyi, A.; Kersten, M.; Adams, F. *Anal. Chem.* **2004**, *76*, 6786–6791.

(9) Nöhammer, B.; David, C.; Burghammer, M.; Riekel, C. *Appl. Phys. Lett.* **2005**, *86*, 163104.

(10) Jochum, K. P.; et al. *Geostand. Newsl.* **2000**, *24*, 87–133.

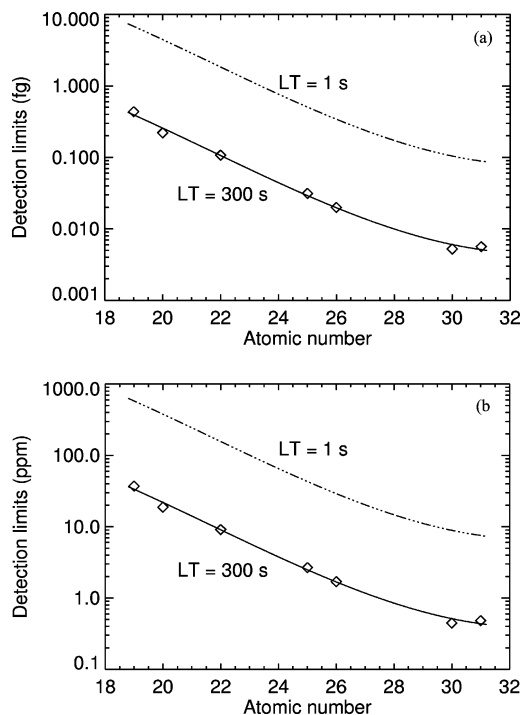


**Figure 3.** (a) Absolute and (b) relative detection limits (DLs) measured at the ESRF ID13 microprobe using a geological reference material (MPI-DING/ATHO<sup>7</sup>), corresponding to a measuring time of 300 and 1 s (dashed curve), respectively. The beam size used was 220 nm  $\times$  170 nm (horizontal  $\times$  vertical, full width at half maximum (fwhm)), excitation energy = 12.7 keV.

ppm (Zn). The statistical uncertainties of the indicated DL values are comparable with the size of the indicated symbols; the indicative line representing the interpolated detection limits for a live time of 1 s (denoted by the dashed curve in Figure 3) was calculated based on the 300 s measurement.

The nano-XRF experiments were performed in air with Stardust Track No. C2044,0,37 enclosed in a triangular slice of the original aerogel matrix (with a thickness of  $\sim 200 \mu\text{m}$ ), wherein it was captured in space (within a so-called keystone). All measurements described below were performed at the excitation energy of 12.7 keV, which is sufficient for the excitation of elements with atomic numbers  $Z \leq 34$  (Se), using sensitive K-line excitation. At the same time, at this incident energy, the excitation of Pb L-lines is avoided, which could otherwise generate lead background signals that originate from shielding materials.

The generated XRF radiation was collected using two VORTEX-EX detectors that were placed on both sides of the sample in the horizontal plane, each at an angle of  $90^\circ$ , with respect to the incoming nanobeam. This dual detector arrangement in a close-coupled geometry not only increased the detected intensity by a factor of 2, but, more importantly, it limited the required angular scan range for the XRF tomography scan to  $180^\circ$  instead of a full rotation scan of  $360^\circ$ . The angular step for the sinograms was  $4.5^\circ$ . After each rotation step, a fast XY scan was performed first, to optimize the sample positioning before the actual projection scan. At each angle, full 2D XRF maps with dimensions of  $3.3 \mu\text{m} \times 4.1 \mu\text{m}$  were recorded, in steps of 100 nm in both directions (XY), using a live time of 1 s per pixel. The chosen 100 nm scanning step size represents an optimal  $2\times$  oversampling of the beam size during the data collection. The required scanning time

was  $\sim 2100$  s per view, yielding a total time for the 3D measurement of 26.3 h.

**XRF Spectral Evaluation.** The raw XRF spectra were converted into elemental net peak intensities using the nonlinear least-squares fitting software package AXIL/MICROXRF2. This software package is dedicated to the accurate deconvolution of large numbers of energy-dispersive XRF spectra collected during micro-XRF scans, including background subtraction and the elimination of peak overlap and other spectral artifacts, such as detector escape and sum peaks.<sup>11</sup>

**Correction for Vertical Sample Drift and Vertical/Horizontal Position.** All off-line corrections discussed below are based on the recorded most-intense 2D XRF elemental maps derived from the Fe-K  $\alpha$  signal. The correction procedure for the submicrometer vertical sample positioning inaccuracies observed during the nano-XRF scan is based on three steps, including (1) correction for slow vertical sample drift during the scan, which could be observed for a few projection angles; (2) correction for submicrometer vertical shifts; and (3) correction for submicrometer horizontal shifts of the sample that are mainly caused by rotation axis imperfections. By correlating the subsequent Fe-K  $\alpha$  images corresponding to the different rotation angles that define the tomographic views, the positioning uncertainties described in points (1)–(3) could be corrected with sufficient accuracy to allow for full 3D reconstruction.

**Vertical Drift Correction.** At each observation angle  $\theta_i$ , the vertical size ( $V_{\text{Size},i}$ ) of the Fe-K  $\alpha$  image was determined as follows. The number of rows in the image that contained at least one pixel with higher intensity than a given threshold value was assumed as the vertical size. A threshold value of  $I_{\text{min}} + (I_{\text{max}} - I_{\text{min}})/10$  was used in our correction, with  $I_{\text{min}}$  and  $I_{\text{max}}$  being the minimum and maximum pixel values over all rotation angles for the Fe-K  $\alpha$  maps. The angles with the smallest vertical size ( $V_{\text{Size,min}}$ ) correspond to vertically undistorted (no vertical sample drift) images. All vertically elongated 2D images, corresponding to vertical sample drift during the scan, were corrected in vertical size using a factor  $V_{\text{Size,min}}/V_{\text{Size},i}$ . An example of a vertically stretched image and a nondistorted image is given in Figure 4a. The vertical profiles show the horizontally integrated intensities of pixels for each row that have intensities above a given threshold value. Based on these vertical profiles, correction can be applied for those images which exhibit vertical sample drift by correlating their vertical profiles with those from neighboring undistorted images.

**Vertical Position Correction.** A rotation around a vertical axis preserves the vertical size and the vertical position of an object. Because of (unintended) submicrometer vertical shifts of the rotation axis during the rotational scanning step, this vertical position correlation is lost between the recorded views. When a specific horizontal line within the 2D image can be identified and moved to a specific fixed vertical position, then the vertical position of the image can be corrected. The rows of a 2D map with at least one pixel value above a chosen threshold will form a subset of the total image, establishing the vertical edges of the particle. After the vertical drift correction step (see previous section), the vertical size defined by this subset is constant over all observation

(11) Vekemans, B.; Janssens, K.; Vincze, L.; Adams, F.; Van Espen, P. *X-ray Spectrom.* **1994**, *23*, 278–285.

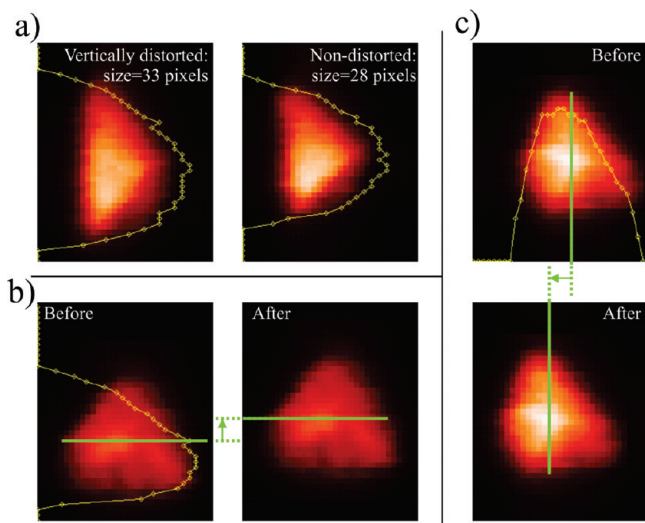


**Figure 4.** Fe–K  $\alpha$  two-dimensional (2D) maps of the terminal particle of cometary impact track Stardust No. C2044,0,37, illustrating the procedures for the three corrections performed: (a) vertical drift (size) correction, showing the vertically stretched image (left panel) and the nondistorted image (right panel); (b) vertical position correction, before vertical position correction (left panel) and after vertical position correction (right panel); and (c) horizontal position correction before horizontal position correction (upper panel) and after horizontal position correction (bottom panel).

angles. By shifting the central row of this image subset to the central row of the image frame, the particle is placed in the vertical center of the corrected image, thus correcting for the vertical shifts induced by submicrometer rotation axis inaccuracies (see Figure 4b).

**Horizontal Position Correction.** The horizontal projection of a point inside an object, as a result of a rotation around a vertical axis, follows a sinusoidal curve. The sines for all points in a horizontal plane form a sinogram. Shifting the rotation axis within the sample only changes the amplitude and phase of the sines in the tomographic sinograms, because the sum of two sine functions with equal periods is a new sine with that period. For the current tomographic dataset, the horizontal correlation between different angles is lost due to rotation stage inaccuracies on the submicrometer scale. However, if the horizontal positions are referred to a reference point inside the sample, the sinogram, with respect to a rotation around a vertical axis through that reference point, can be obtained. Such a reference point can be the center of mass of the particle. In our correction algorithm, the horizontal axis of symmetry was used to approximate the horizontal position of the center of mass. For a convex, approximately symmetric shape (such as that represented by the comet coma particle), the horizontal center of symmetry approximates well the horizontal position of the center of mass. During the horizontal position correction, the horizontal symmetry center of the measured image is shifted to the center of the corrected image frame, and the reconstruction was performed as if the rotation axis went through the center of the particle. To correct the horizontal position in this way, a procedure similar to that used for the vertical position correction can be followed, but now the image columns are used, instead of the rows. All the columns in the 2D maps with at least one pixel value above a certain threshold form a subset of the image. By shifting the central column of this subset to the central

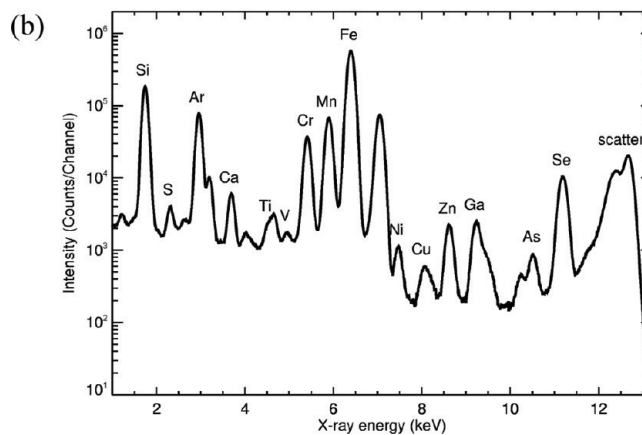
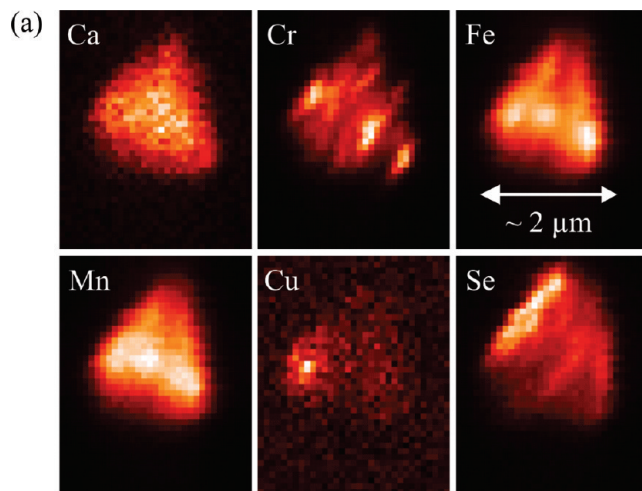


**Figure 5.** Nano-XRF mapping: (a) scaled 2D maps for the most abundant major/minor and trace elements in the XRF spectra of the terminal particle of cometary impact track Stardust No. C2044,0,37 (horizontal dimension =  $33 \times 100$  nm, vertical dimension =  $44 \times 100$  nm) and (b) summary spectrum of all individual XRF pixel spectra of a projection on the terminal particle of cometary impact track Stardust No. C2044,0,37.

column of the corrected image frame, the horizontal position can be corrected, as illustrated in Figure 4c.

The image processing/visualization and the specific reconstruction algorithms previously described have been implemented using the Interactive Data Language (IDL) software, version 6.3, by ITT Visual Information Solutions.

## RESULTS AND DISCUSSION

**Two-Dimensional Nano-XRF Projection Maps.** In the case of the full 3D extension of XRF computed nanotomography that is presented below, full-field images of the elemental distributions were recorded from the sample volume by *XY* scanning at different observation (azimuthal) angles. The obtained projection images were used to obtain full 3D information on the elemental distributions on a submicrometer-resolution level within this unique cometary material after tomographic reconstruction.

As an example, the 2D maps at a given observation angle for the most abundant detectable major/minor and trace elements of the coma particle from comet 81P/Wild2 are given in Figure 5, together with the sum spectrum of all individual pixel spectra within that projection. Based on the 2D elemental maps, the

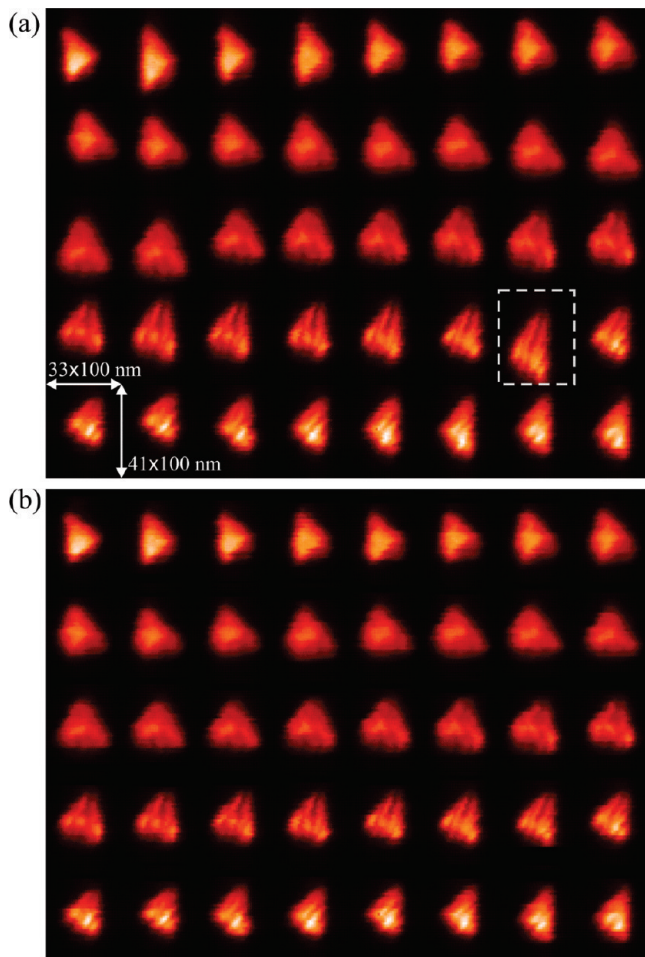


**Figure 6.** Fe–K  $\alpha$  2D maps of the terminal particle of cometary impact track Stardust No. C2044,0,37, for an angular range of 180° (4.5°/step): (a) uncorrected images and (b) corrected images. An example for a highly distorted image is marked by a dashed box.

terminal particle clearly exhibits heterogeneities on the submicrometer level for several detectable elements, including chromium, iron, copper, and selenium. The Fe–K  $\alpha$  2D nanoscopic XRF maps recorded at each rotation angle are given in Figure 6a. After each rotation, mainly because of the mechanical instabilities of the rotation axis, the sample position typically shifted over a range of 100–500 nm, which is relatively large, compared to the sample size and the spatial resolution defined by the X-ray beam size. The induced inaccuracies in a relative sample position were partially corrected during the tomographic scan by applying an automated XRF fast-scanning algorithm to center the particle in the nanobeam after each rotational movement. This automated particle centering procedure, relative to the X-ray nanobeam, was performed each time before starting a 2D full-field projection scan. Consequently, the vertical and horizontal positions of the sample in the obtained 2D XRF maps corresponding to the different observation angles are not correlated. Moreover, at several observation angles, a vertical drift of the sample occurred, because of gravitational relaxation of the sample stage, which resulted in images of the particle that were elongated along the vertical axis (see, for example, the dashed image in Figure 6a). Figure 6b shows the vertical size/position corrected images that were used to perform the tomographic reconstruction. The following three

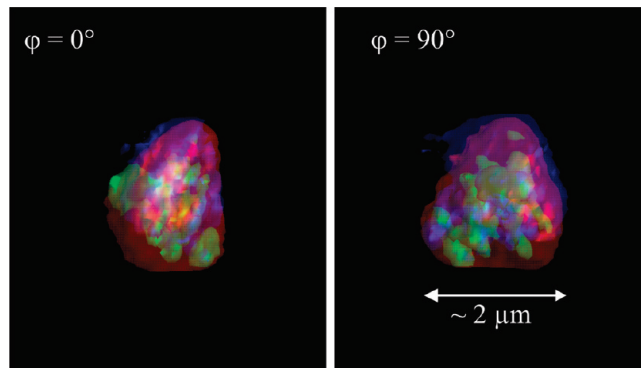


**Figure 7.** Reconstructed low-intensity isosurface composite images for different azimuthal viewing angles: red denotes iron, green represents chromium, and blue indicates selenium.

corrections were necessary at each angle to obtain Figure 6b: (1) vertical size, (2) vertical position, and (3) horizontal position correction.

The applied corrections (see the Experimental Section) were determined based on the Fe–K  $\alpha$  XRF maps that showed the best counting statistics, because the highest count rates were obtained for this element. The established corrections were then applied to all elements in the next step. The corrections used are detailed in the Experimental Section. The effect of all corrections on the Fe–K  $\alpha$  2D maps is illustrated in Figure 6b. As a result of the applied corrections, the (random) vertical and horizontal movements of the particle within the image frame were corrected and a constant vertical size was obtained.

**Reconstructed 3D View.** The elemental intensity profile at a certain particle height (corresponding to a given row in the 2D maps) over all rotation angles provide the elemental sinogram for a given cross section through the sample. The reconstructed elemental distributions within this virtual cross section of the particle, corresponding to a selected height, could be obtained by applying a back-projection algorithm on the (height-dependent) sinogram.<sup>12,13</sup> The combination of the reconstructed cross sections (slices) for all heights enables the visualization of the complete 3D view of elemental distributions in the terminal particle within the investigated cometary track. A pseudo-color (RGB) composite image of the low-intensity isosurface distributions of iron (red), chromium (green), and selenium (blue) for different azimuthal viewing angles is given in Figure 7. Heterogeneous elemental distributions inside the terminal particle are visualized in 3D on a nanoscopic level (see, e.g., the high-intensity isosurface for chromium).

The documented inhomogeneous distribution of elements in the terminal particle helps to understand the nature of the studied material and distinguish between artificial elemental concentrations and that of the chemistry of the captured cometary particle, which is essential for the reconstruction of the comet bulk chemistry.<sup>3</sup> It was shown that some elements, such as copper, zinc, and gallium, show substantial enrichment over chondritic composition (compared to materials that dominate interplanetary dust and the matrix of primitive carbon-rich meteorites).<sup>3</sup> The

(12) Russ, J. C. *The Image Processing Handbook*, 2nd Edition; CRC Press: Boca Raton, FL, 1994.

(13) Park, S.; Schowengerdt, R. *Comput. Vision, Graphics Image Process.* **1983**, *23*, 256.

observed selenium concentrations show the largest variation of hot-spot analyses documented by Flynn et al.<sup>3</sup> Both increased values over chondritic composition and the variable elemental concentrations from hot-spot analyses could be explained by the observed 3D distribution of elements. The trace element content of the aerogel used is highly variable and complex. Elemental concentrations that are on the trace element level in the original aerogel foam can be increased up to main elemental concentrations if the aerogel is substantially compressed or melted. The terminal particle studied in this work shows a selenium enrichment surrounding the top of the grain, which is a clear indication for compressed aerogel in front of the impacted cometary dust particle. The selenium distribution clearly forms a shell around the particle that does not originate from the particle itself. XRF measurements on the aerogel collectors used to capture the particles revealed the presence of trace levels of selenium, which represents the most likely origin of the Se lines within the measured nano-XRF spectra. The detected Se-rich external layer surrounding the particle is attributed to the partial melting and subsequent solidification of the aerogel around the terminal particle, as a result of the high-speed impact of the comet coma particle. During its high-speed capture in the aerogel collector, the particle is decelerated from its original relative speed of 6.1 km/s, melting and compacting the aerogel matrix along its penetration path. This leads to the increased density of the aerogel around the terminal particle and also increased the volume concentration level of trace elements present in the aerogel (such as selenium), resulting in the observed selenium-rich shell.

The platelike 3D distributions of chromium and iron in the terminal grain resembles the structure of cryptocrystalline olivine–pyroxene chondrules. This interpretation is further supported by recent findings of chondrule-like objects in Wild2 (see the work of Nakamura et al.<sup>14</sup>), which is a further strong argument for large-scale mixing within the protoplanetary disk.

As demonstrated by the aforementioned example on this unique cometary material, the submicroscopic 3D reconstruction of trace-level elemental distributions within this 2  $\mu\text{m}$  individual particle not only reveals the heterogeneous nature of the analyzed cometary grain, but also enables one to distinguish between elemental constituents originally present in the cometary matter and those present as impurities within the embedding aerogel host matrix.

## CONCLUSIONS

Fully three-dimensional (3D), nondestructive, trace-level elemental nanoimaging was demonstrated based on X-ray fluores-

cence (XRF) nanotomography at the Microfocus Beamline (ID13) of the European Synchrotron Radiation Facility (ESRF). The demonstrated technique represents a significant generalization of the well-known principle of XRF microtomography, by applying (1) nanometer-sized X-ray beams ( $\sim 200$  nm) and (2) collecting two-dimensional (2D) scanning XRF maps for each tomographic view, instead of one-dimensional (1D) linear scans. This opens the possibility for (1) obtaining fully 3D elemental distributions from the entire examined sample microvolume, instead of a single sample cross section, and (2) applying correction procedures for submicrometer sample positioning inaccuracies, which can be considerable during scans with nanoscopic step sizes. Our submicrometer XRF tomography experiment also demonstrated local XRF tomography for the first time, given that the investigated microvolume was embedded in a low-density host material (aerogel).

The nondestructive submicrometer 3D elemental imaging method was demonstrated on unique cometary matter from comet 81P/Wild2 with  $\sim 200$  nm spatial resolution, limited by the applied beam size. The reconstructed nano-XRF tomography dataset revealed the heterogeneous nature of elemental distributions inside the investigated cometary grain, which could be visualized in 3D on a nanoscopic level (100 nm voxel size obtained by a factor 2 oversampling during the scans).

As demonstrated, nanoscopic XRF tomography is possible, but not yet routinely. Generally speaking, improved sample positioning systems are needed; a small sphere of confusion for the rotation axis is especially a necessity. Sample position control systems at the nanometer accuracy level must be developed to make nano-XRF tomography at synchrotron sources a standard 3D elemental imaging tool.

## ACKNOWLEDGMENT

The authors thank the NASA Stardust team (especially Don Brownlee and Peter Tsou) and the Jet Propulsion Laboratory for providing these unique samples. F.E.B. wishes to acknowledge the support of George Flynn, Andrew Westphal, and Mike Zolensky during the PET phase. John Morse is gratefully acknowledged for providing the ED-XRF detector systems for the experiment. G.S. is supported by a post-doctoral fellowship from the Research Foundation-Flanders (FWO-Vlaanderen, Belgium), and B.V. is supported by the IAP6 Programme by BELSPO. F.E.B. and S.S. are grateful for funding from the German Science Foundation (DFG).

Received for review March 9, 2009. Accepted June 4, 2009.

AC900507X

(14) Nakamura, T.; Noguchi, T.; Tsuchiyama, A.; Ushikubo, T.; Kita, N. T.; Valley, J. W.; Zolensky, M. E.; Kakazu, Y.; Sakamoto, K.; Mashio, E.; Uesugi, K.; Nakano, T. *Science* **2008**, *321*, 1664–1667.